ADVANCING EARTH AND SPACE SCIENCES

Geophysical Research Letters

RESEARCH LETTER
10.1029/2023GL106439

The Hunga Tonga-Hunga Ha'apai Volcanic Eruption as Seen in Satellite Microwave Observations and MiRS Temperature Retrievals

Yong-Keun Lee[1,2], Neil Hindley[3], Christopher Grassotti[1,2], and Quanhua (Mark) Liu[2]

[1]Earth System Science Interdisciplinary Center, Cooperative Institute for Satellite Earth System Studies, College Park, MD, USA, [2]Center for Satellite Applications and Research, National Oceanic and Atmospheric Administration, National Environmental Satellite Data Information Service, College Park, MD, USA, [3]Center for Space, Atmospheric, and Oceanic Science, University of Bath, Claverton Down, UK

Key Points:

- Microwave observations from multiple satellites capture stratospheric waves from the Tonga eruption, including Lamb and gravity waves
- MiRS atmospheric temperature retrievals also resolve wave perturbations in the stratosphere after the eruption
- The Lamb wave and the lead gravity wave show no apparent phase change with height, whereas the trailing gravity waves do

Correspondence to:
Y.-K. Lee,
ylee1218@umd.edu

Citation:
Lee, Y.-K., Hindley, N., Grassotti, C., & Liu, Q. (2023). The Hunga Tonga-Hunga Ha'apai volcanic eruption as seen in satellite microwave observations and MiRS temperature retrievals. *Geophysical Research Letters*, *50*, e2023GL106439. https://doi.org/10.1029/2023GL106439

Received 20 SEP 2023
Accepted 20 NOV 2023

Author Contributions:

Conceptualization: Yong-Keun Lee
Data curation: Yong-Keun Lee
Formal analysis: Yong-Keun Lee
Funding acquisition: Christopher Grassotti, Quanhua (Mark) Liu
Investigation: Yong-Keun Lee
Methodology: Yong-Keun Lee
Project Administration: Christopher Grassotti, Quanhua (Mark) Liu
Resources: Yong-Keun Lee
Software: Yong-Keun Lee, Neil Hindley
Supervision: Yong-Keun Lee
Validation: Yong-Keun Lee
Visualization: Yong-Keun Lee
Writing – original draft: Yong-Keun Lee
Writing – review & editing: Yong-Keun Lee, Christopher Grassotti, Quanhua (Mark) Liu

Abstract The strongest volcanic eruption since the 19th century occurred on 15 January 2022 at Hunga Tonga-Hunga Ha'apai, generating unprecedented atmospheric waves not seen before in observations. We used satellite microwave observations from (a) Advanced Technology Microwave Sounder (ATMS) on board the National Oceanic and Atmospheric Administration (NOAA)-20 and the Suomi-National Polar-orbiting Partnership (SNPP) and (b) Advanced Microwave Sounding Unit (AMSU)-A on board Meteorological operational satellite (MetOp)-B/MetOp-C to study these waves in the stratosphere immediately after the eruption. The NOAA Microwave Integrated Retrieval System (MiRS) was applied to these microwave observations to produce atmospheric temperature profiles. The atmospheric Lamb wave and fast-traveling gravity waves are clearly revealed in both the brightness temperatures and the MiRS retrieved temperatures, revealing their vertical phase structures. This study is the first attempt to perform a detailed analysis of the stratospheric impact of the Tonga eruption on operational satellite microwave observations and the corresponding MiRS retrievals.

Plain Language Summary The strongest volcanic eruption since the 19th century occurred on 15 January 2022 at Hunga Tonga-Hunga Ha'apai. The microwave instruments onboard the currently operational satellites observed the area in the vicinity of the eruption. The eruption impacts were most obvious at high altitudes (the stratosphere) in the observed microwave brightness temperatures. Additionally, atmospheric temperature profiles have been retrieved using the satellite measured microwave brightness temperatures. The retrieved atmospheric temperature fields also show the impacts of the volcanic eruption in the stratosphere. This study is the first attempt to perform a detailed analysis of the impact of the Tonga volcanic eruption using operational satellite microwave observations and the corresponding retrievals.

1. Introduction

On 15 January 2022 the strongest explosive volcanic eruption since the 19th century occurred at Tonga Hunga-Hunga Ha'apai (20.536°S and 175.382°W, hereafter Tonga). The strength of the Tonga volcanic eruption was comparable to that of Krakatoa in 1883 (Matoza et al., 2022; Schoeberl et al., 2022; Wright et al., 2022). For the Krakatoa eruption, the observations were mainly from the surface. Fortunately, in the case of the Tonga eruption, there exists a much improved global observation network that includes a large number of measurements from multiple satellites. Many of the publications on the Tonga volcanic eruption utilized satellite measurements. For example, Carr et al. (2022) calculated the approximate height of the volcanic eruption plume using infrared and visible wavelength observations from geostationary orbiting satellites, GOES-17 and Himawari-8. Wright et al. (2022) and Matoza et al. (2022) used low earth orbit and geostationary orbit infrared wavelength measurements to find the atmospheric wave features generated by the Tonga volcanic eruption combined with surface measurements.

In this study, National Oceanic and Atmospheric Administration (NOAA)-20 and the Suomi National Polar-orbiting Partnership (SNPP) Advanced Technology Microwave Sounder (ATMS) measurements are used in the analysis, as are measurements from the Meteorological operational satellite (MetOp)-B/MetOp-C Advanced Microwave Sounding Unit (AMSU)-A. Furthermore, the Microwave Integrated Retrieval System (MiRS) algorithm has been applied to the satellite microwave radiance measurements to investigate what impact, if any, is revealed in the

retrieved atmospheric temperature profiles due to the volcanic eruption on 15 January 2022. Since MiRS provides height-resolved atmospheric temperature retrievals for every point in ATMS measurements, it would lead us to effectively create a 3-D observation in temperature.

Section 2 describes the data and methods, Section 3 presents the results of atmospheric waves generated by the Tonga volcanic eruption observed by the satellite microwave measurements and the MiRS retrieved atmospheric profiles, and Section 4 contains a summary and discussion.

2. Data and Methods

NOAA-20/SNPP ATMS and MetOp-B/MetOp-C AMSU-A measured brightness temperatures and the MiRS retrieved atmospheric temperature profiles are analyzed in this study. ATMS is a microwave radiometer having 22 channels with temperature sounding (V band) and humidity sounding (G band) capabilities. AMSU-A is used with the Microwave Humidity Sounder (MHS) in MiRS and their channel combination is similar to ATMS including V-band (AMSU-A) and G-band (MHS), respectively. Both MetOp-B and MetOp-C satellites contain the combination of AMSU-A and MHS. Since the weighting function peaks of the V band channels in ATMS and AMSU-A are located in the stratosphere and troposphere (in the troposphere for *G* band channels), it is expected that the brightness temperatures measured by ATMS and AMSU-A may reveal the impact of the Tonga volcanic eruption on these atmospheric layers.

The MiRS algorithm retrieves atmospheric temperature/water vapor and hydrometeor vertical (about 100 pressure layers from the surface to 0.01 hPa) profiles during the main 1-dimensional variational retrieval procedure using the satellite microwave measurements as input. The MiRS atmospheric temperature profile is retrieved based on the measurements in the ATMS and AMSU-A channels, therefore, any impact of the Tonga volcanic eruption on the satellite measured microwave brightness temperatures should also be found in the MiRS retrieved atmospheric temperature profiles. Boukabara et al. (2011, 2013) described the MiRS algorithm and further technical details can be found in these publications. ATMS and AMSU-A have 96 and 90 fields of view (FOVs) per scan line, respectively, and both ATMS and AMSU-A consist of approximately 30,000 scan lines each day.

Based on the magnitude of the eruption and the previous published analyses, we assumed that the wave patterns generated by the eruption will be detectible in some of the microwave measurements. The approach to detecting and analyzing the waves was to first determine the local perturbation (departure from the local mean value) of the measurements. In order to characterize the wave (perturbation) pattern generated by the Tonga eruption from the ATMS and AMSU-A measured brightness temperatures and the MiRS retrieved atmospheric temperatures, 3×3 neighboring FOVs (or pixels) were averaged horizontally to reduce local scene variability and then a 2-dimensional fifth order polynomial curve fit was applied to these 3×3 averaged values. The difference between the 3×3 averaged value and the polynomial curve fitted value was considered the perturbation of the given variables.

The MiRS retrieved atmospheric temperature profile has 100 layers, while ATMS and AMSU-A have 22 and 15 channels, respectively. The difference calculation (local 3×3 FOV average minus the polynomial curve fit) was applied for each pressure layer of atmospheric temperature profiles and for each channel of ATMS and AMSU-A brightness temperatures to determine the perturbation.

The formula for 2-D polynomial curve fit is given below.

$$\begin{aligned}\text{fitresult}(x, y) = {} & p00 + p10 * x + p01 * y + p20 * x^2 + p11 * x * y \\ & + p02 * y^2 + p30 * x^3 + p21 * x^2 * y + p12 * x * y^2 + p03 * y^3 \\ & + p40 * x^4 + \mathrm{p}31 * x^3 * y + p22 * x^2 * y^2 + p13 * x * y^3 \\ & + p04 * y^4 + p50 * x^5 + p41 * x^4 * y + p32 * x^3 * y^2 \\ & + p23 * x^2 * y^3 + p14 * x * y^4 + p05 * y^5\end{aligned} \tag{1}$$

x represents longitude, y latitude, pij polynomial coefficients, i and j are integer exponents for x and y, respectively.

The observation time difference between the 9 FOVs (3×3) are less than 10 s for both ATMS and AMSU-A. Horizontal resolution for an FOV is about 32 km (48 km) at nadir for NOAA-20/SNPP ATMS (Metop-B/C AMSU-A). 2-D polynomial was applied to 3×3 FOV averaged brightness temperatures or atmospheric

temperatures using the geolocation information. Brightness temperatures or atmospheric temperatures calculated using Equation 1 are considered the background used to remove limb-brightening effect in the measurements following the previous studies. In previous studies (Alexander & Barnet, 2007; Wright et al., 2022; Wu, 2004), the polynomial was used as the background of the satellite measurements to study gravity waves, since the limb-brightening effect at the temperature sounding channels (~57 GHz) is well captured by the brightness temperatures calculated using the polynomial.

3. Results

3.1. Tonga Impact on NOAA-20/SNPP ATMS and MetOp-B/MetOp-C AMSU-A Measurements

Atmospheric pulses are known to be transmitted after a large explosion such as a volcanic eruption (Press & Harkrider, 1966). The atmospheric waves generated by a large explosion include Lamb waves and internal gravity waves. The phase speed of the Lamb wave is known to be faster than the internal gravity waves (Wright et al., 2022). The other difference between the Lamb wave and most of the gravity wave packet is whether the motion of particles is vertically in phase (e.g., Lamb waves, Bretherton, 1969) or not. The lead gravity wave among the trailing internal gravity waves has slower phase speed than the Lamb wave, however, its vertical wave number is close to zero indicating that the atmospheric wave is in phase vertically which is also a characteristic of the Lamb wave (Wright et al., 2022). The trailing gravity waves (in this study, the pixels whose phase speed is less than 200 m/s) show slower phase speed than the lead gravity wave and they have vertical phase change in the atmospheric perturbations.

Figure 1 shows the time evolution of the atmospheric waves generated by the Tonga eruption using NOAA-20/SNPP ATMS channel 15 (descending orbits) and MetOp-B/MetOp-C AMSU-A channel 14 (ascending orbits) brightness temperature perturbations. These channels have weighting functions peaking in the upper stratosphere at 40–45 km. The atmospheric waves generated by the eruption propagate in all directions and there is approximately a one-hour difference between (a) and (b) and between (c) and (d), respectively. The concentric pattern of the brightness temperature perturbations moving outward with time is clear in both the ATMS and AMSU-A measurements. NOAA-20/SNPP and MetOp-B/MetOp-C are polar orbiting satellites with a temporal observation frequency of about two times per day for a given region in the mid and low latitudes. This results in some orbits of NOAA-20/SNPP ATMS and MetOp-B/MetOp-C AMSU-A clearly revealing the concentric perturbation pattern while other orbits do not due to observation time and location differences.

The stratosphere is thermally stable (i.e., temperature increases with height), therefore, the buoyancy effect provides a favorable environment for the horizontal perturbation propagation in the atmosphere. Conversely, average atmospheric vertical stability in the troposphere is weaker relative to the stratosphere, which results in a damping of the wave. Therefore, it is more difficult to detect the atmospheric temperature disturbances generated by the Tonga volcanic eruption at channels whose weighting function peaks are located in the troposphere. In this study we restrict the analysis to stratospheric sounding channels and to atmospheric pressure layers less than 50 hPa. An analysis of the perturbation as a function of channel shows that the wave amplitude is the largest at channel 15 for ATMS and at channel 14 for AMSU-A which have the weighting function peak at 40–45 km based on the U.S. standard atmosphere (Zhang et al., 2017; Zou & Qian, 2016). This wave amplitude decreases as the weighting function peak altitude becomes lower which will be discussed below and shown in Figure 2b.

The Lamb wave can be identified as the perturbation located most distant to the north and south from the Tonga volcano location in Figure 1 (identified in the figure by the set of two black-curved lines indicated by the black right-pointing triangles). This location was also identified in Wright et al. (2022) who indicated that the trigger source for the atmospheric wave occurred at about 4:28 UTC 15 January 2022 based on the back-projection of surface pressure data. The outermost line on both north and south sides in each panel of Figure 1 corresponds to a phase speed of 330 m/s assuming the wave was generated by the Tonga eruption at the initial trigger occurrence. The second outermost line corresponds to a phase speed of 300 m/s. These two outermost curved lines represent the likely bounds of the Lamb wave. The third outermost curved line and the innermost curved line correspond to phase speeds of 270 and 230 m/s, respectively (two black-curved lines indicated by the red right-pointing triangles), and represent the likely bounds of the lead gravity wave which was also generated at the time of the initial eruption trigger occurrence. The approximate observation times are indicated in each panel for Figure 1 for both the outermost (Lamb) wave and subsequent lead (gravity) wave. For example, the Lamb wave is clearly observed

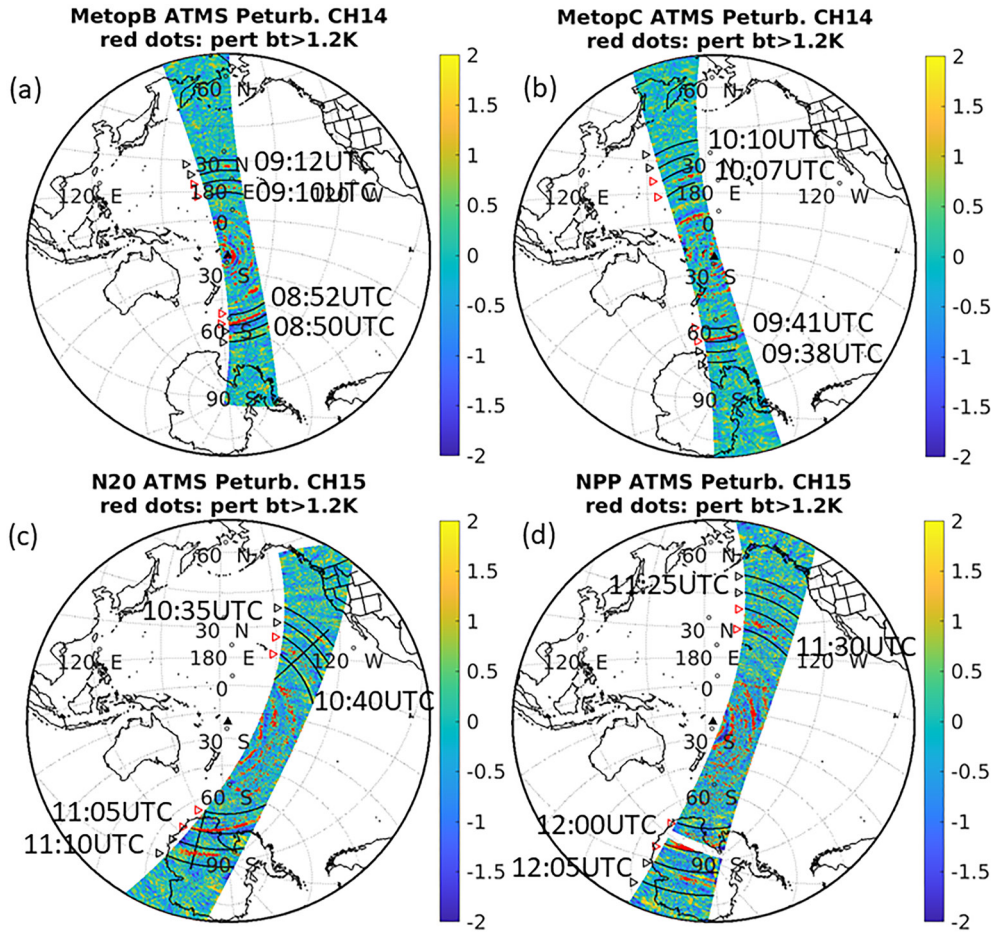

Figure 1. The local perturbations in observed microwave brightness temperatures from an ascending orbit of (a) MetOp-B AMSU-A channel 14, (b) MetOp-C AMSU-A channel 14, a descending orbit of (c) NOAA-20 ATMS channel 15, and (d) SNPP ATMS channel 15 on 15 January 2022. The black triangle at the center for each panel is the Tonga volcano location. The outermost black-curved lines from the Tonga volcano location correspond to a phase speed of 330 m/s assuming that the perturbation has been generated at the time and location of initial volcanic eruption. From the second outermost black-curved lines to the innermost lines, the phase speeds are 300, 270, and 230 m/s, respectively. The time information in each panel indicates the approximate observation time for the Lamb wave (between 300 m/s and 330 m/s indicated by black right-pointing triangles) and for the lead gravity wave (between 230 m/s and 270 m/s indicated by red right-pointing triangles). Red dots indicate the pixels where the brightness temperature perturbation is larger than 1.2 K. Two black-straight lines in (c) are used in Figure 2a to show perturbations following each line.

in the NOAA-20 ATMS measurements at approximately 10:35 UTC to the north of Tonga and at around 11:10 UTC to the south (i.e., a phase speed between 300 and 330 m/s) in Figure 1c. While the lead gravity wave is observed at around 10:40 UTC to the north (weakly observed) of Tonga and at approximately 11:05 UTC to the south (i.e., a phase speed between 230 and 270 m/s). The phase speeds of the Lamb wave and the lead gravity wave shown in the microwave measurements of this study are very consistent with those seen in the infrared measurements (Wright et al., 2022).

In Figure 2a, perturbations of brightness temperature are shown with phase speed following the two straight-black lines in Figure 1c. The peaks are clear between 310 and 320 m/s and between 250 and 270 m/s for the Lamb wave and the lead gravity wave, respectively.

Since some orbits do not clearly show the perturbation associated with the Lamb wave (due to observation time and location characteristics of the polar orbits), NOAA-20 orbits are used here to show the vertical phase structure of both microwave brightness temperature perturbations and MiRS retrieved temperature perturbations. In order to characterize the perturbation spectral or vertical dependence, multiple FOVs were selected and averaged, with the goal of obtaining a mean spectral or vertical profile associated with the Lamb wave, the lead gravity

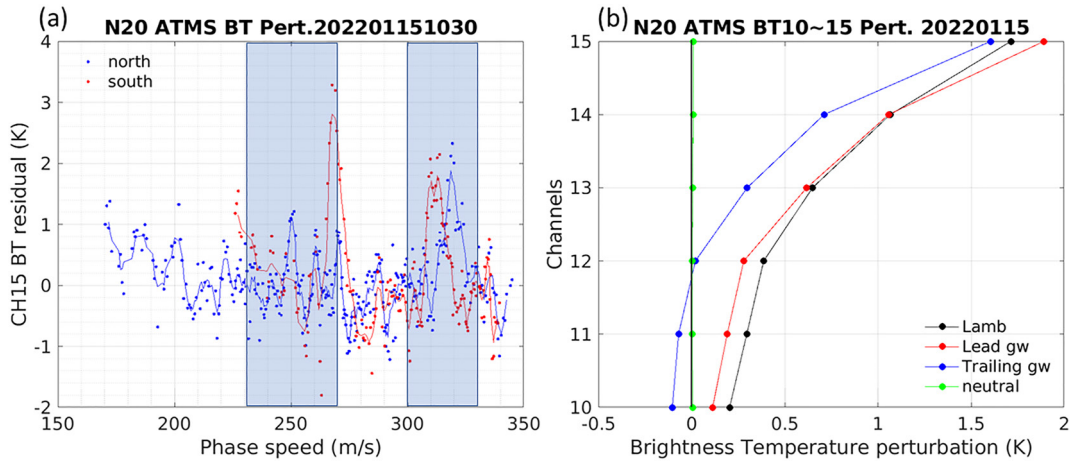

Figure 2. (a) NOAA-20 ATMS brightness temperature (channel 15) perturbations following two straight-black lines that extend from the Tonga eruption location in Figure 1c. Perturbation data are shown for the northern and southern lines using blue and red symbols, respectively. The overlapped lines are five pixel moving average for each. Light-blue shaded areas correspond to equal phase speed lines in Figure 1c for the Lamb wave and the first lead gravity wave, respectively. (b) NOAA-20 ATMS brightness temperature perturbation by channels between 10 and 15 for each wave on 15 January 2022. The perturbation curves are based on a selection of pixels (FOVs) in the vicinity of the wave crests. The curve corresponding to "neutral" indicates the FOVs not affected by the volcanic eruption located at distances beyond the fastest moving Lamb wave. The numbers of pixels used in these figures are 362, 597, 696, and 27,376 for the Lamb wave, the lead gravity wave, the trailing waves, and non-atmospheric wave (neutral) area, respectively.

wave, and the trailing gravity waves, respectively. The selection criterion was a perturbation of 1.2 K or larger in ATMS channel 15 for brightness temperature and 1.2 K or larger at 2.5 hPa for atmospheric temperature. In order for an FOV to be selected, these criteria should be met for both brightness temperature and atmospheric temperature. In addition to the temperature perturbation criteria, the FOVs were selected based on spatial location criteria. For the assumed Lamb wave crest, only FOVs located within the bounds defined by the phase speeds between 308 and 319 m/s were included. For the assumed lead gravity wave, only FOVs located within the bounds defined by phase speeds between 240 and 270 m/s were selected. These values are from Wright et al. (2022). For the trailing gravity waves, FOVs with phase speed less than 200 m/s were selected. Finally, to characterize neutral atmospheric conditions unaffected by the Tonga eruption, FOVs corresponding to a phase speed of 350 m/s or greater were selected.

The spectral dependences are shown in the spectral profile of averaged perturbations for ATMS channels 10–15 (Figure 2b). The channel ordering along the vertical axis is in order increasing height of the estimated weighting function peak in each channel, with channel 10 and 15 having weighting function peaks at approximately 90 and 2.5 hPa, respectively. In the stratosphere, the brightness temperature perturbation for the Lamb wave is primarily positive indicating the same phase in the stratospheric layers observed by these channels, with the perturbation magnitude decreasing as the weighting function peak altitude decreases. The high phase speed, large perturbation amplitude, and in-phase vertical structure are consistent with the characteristics of a Lamb wave. Theoretically, the lead gravity wave has the same phase at all altitudes (Fritts & Alexander, 2003; Swenson et al., 2000; Wright et al., 2022). In Figure 2b the vertical structure of the lead gravity wave perturbation shows a similar behavior to that of the Lamb wave, that is the perturbation remains positive with decreasing amplitude in the stratosphere as the altitude decreases (or the weighting function peak lowers from channel 15 to channel 10). With regard to the trailing gravity waves which are located closer to the Tonga eruption location, the vertical perturbation profile shows a very different structure. In this case, there is a shift in sign of the perturbation from positive to negative as one moves to lower altitudes, which is different from the lead gravity wave (Fritts & Alexander, 2003; Swenson et al., 2000; Wright et al., 2022).

The perturbation amplitude of the NOAA-20 ATMS microwave brightness temperature at channel 15 is about 1.7 K for the Lamb wave and about 1.9 K for the lead gravity wave in the wave packet that follows the Lamb wave. The magnitude of perturbations of the Lamb wave and the lead gravity wave both decrease as the altitude decreases (moving from channel 15 to channel 10), with amplitudes of 0.2 and 0.1 K for the Lamb wave and lead

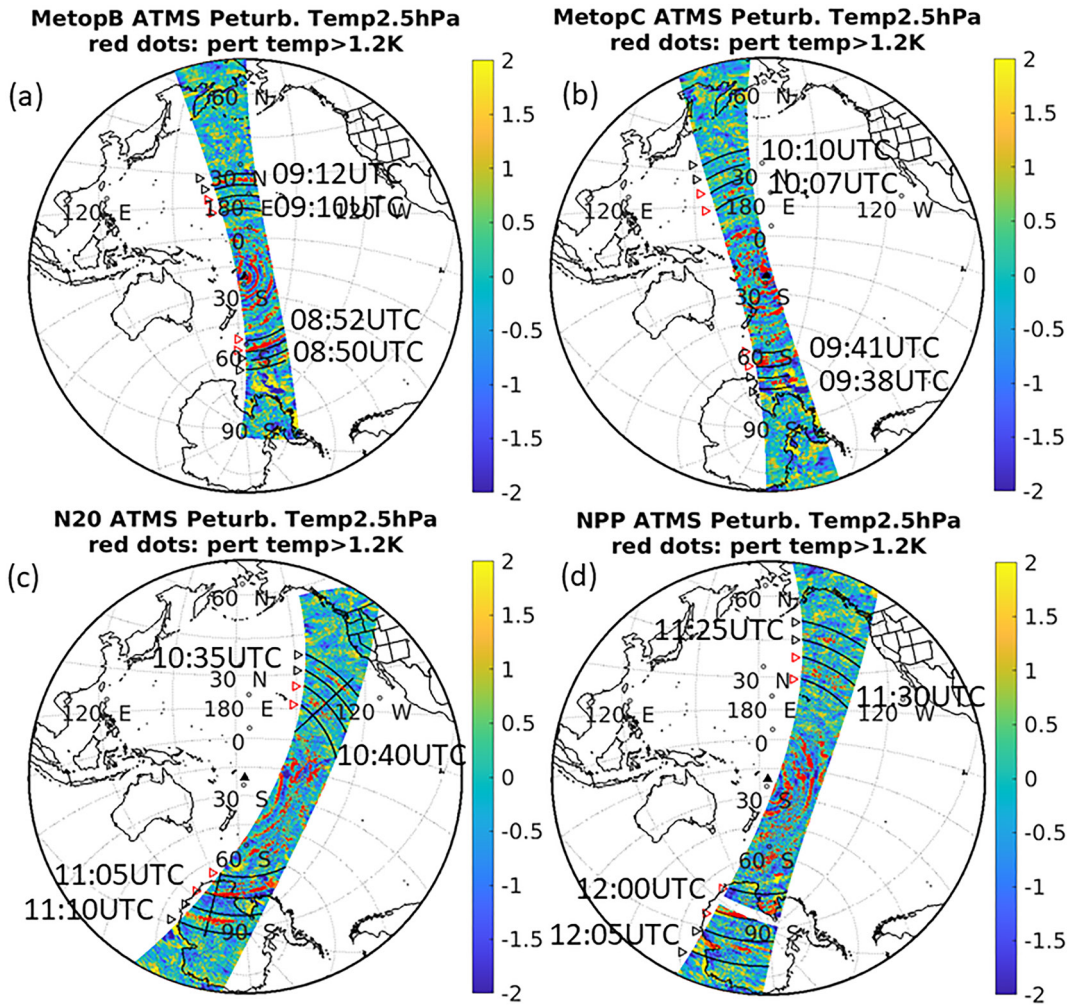

Figure 3. The local perturbations of the MiRS retrieved atmospheric temperature from (a) an ascending orbit of (a) MetOp-B AMSU-A, (b) MetOp-C AMSU-A, a descending orbit of (c) NOAA-20 ATMS, (d) SNPP ATMS at 2.5 hPa on 15 January 2022. The black-curved lines and the time information in each panel are the same as Figure 1. Red dots indicate the pixels where atmospheric temperature perturbation is larger than 1.2 K. Two black-straight lines in (c) are used in Figure 4a to show perturbations following each line.

gravity wave, respectively at channel 10. The trailing gravity waves show a change in perturbation amplitude sign indicative of a change in wave phase, ranging from 1.6 K at channel 15 to approximately −0.1 K at channel 10. The perturbation amplitude increase with height could be partly due to the atmospheric density decrease (Fritts & Alexander, 2003). Although not shown here, the SNPP ATMS and the MetOp-B/MetOp-C AMSU-A brightness temperatures also reveal a similar perturbation vertical structure to that of NOAA-20 ATMS as long as the wave crest is obvious in the orbits. All the FOVs whose distances are far enough from the volcano location not to be affected by the eruption have been selected to show a normal vertical structure of the perturbation. In these cases (green line in Figure 2b), the perturbation of the brightness temperature is close to 0 in all channels.

3.2. Tonga Impact as Seen in MiRS Retrieved Atmospheric Temperatures

Given the results seen in the brightness temperature analysis presented above, it is logical to extend the analysis to the actual atmospheric temperature structure associated with Tonga eruption. In this section, temperature profiles obtained from the MiRS retrieval algorithm are used for the atmospheric analysis. The MiRS retrieval quality has been validated in previous studies (Grassotti et al., 2023; Lee et al., 2022) and validation exercises (Grassotti et al., 2019). The atmospheric temperature perturbation horizontal structure as seen in the MiRS NOAA-20/SNPP ATMS and MetOp-B/MetOp-C AMSU-A 2.5 hPa temperature retrievals is shown in Figure 3. The locations of

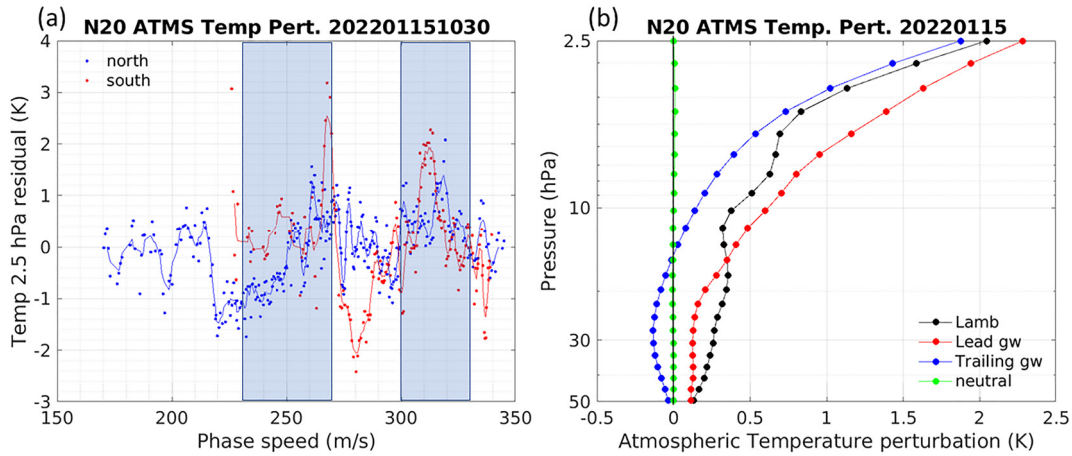

Figure 4. Same as Figure 2 except for MiRS NOAA-20 ATMS retrieved atmospheric temperature perturbation (a) at 2.5 hPa following two straight-black lines in Figures 3c and 3b vertical structure between 2.5 and 50 hPa.

the atmospheric wave patterns correspond well to those seen in the ATMS and AMSU-A brightness temperatures (Figure 1). In Figure 4a, atmospheric temperature perturbations are shown as a function of phase speed following the two black-straight lines in Figure 3c. Similar to the brightness temperature perturbations seen in Figure 2a, the peaks are clear between 310 and 320 m/s and between 260 and 270 m/s for Lamb wave and the lead gravity wave, respectively.

The MiRS retrieved atmospheric temperature perturbation vertical structures at the locations of the Lamb and gravity waves (using the same selection criteria described above for the brightness temperatures) are similar to the brightness temperature spectra (Figure 4b). The perturbation amplitude of the retrieved atmospheric temperature field at 2.5 hPa is about 2.0 K for the Lamb wave and about 2.3 K for the lead gravity wave. These temperature perturbations associated with the Lamb wave and the lead gravity wave are maximized at around 2.5 hPa and decrease steadily down to roughly 50 hPa, where the perturbation amplitude is approximately 0.1 K for both the Lamb and lead gravity wave in Figure 4b. While not shown here, the MiRS retrieved atmospheric temperatures from SNPP ATMS and the MetOp-B/MetOp-C AMSU-A also show similar perturbation vertical structures as those from the NOAA-20 ATMS as long as the wave crest is obvious in the orbits. As in Figure 2b, all the FOVs whose distances are far enough from the volcano location not to be affected by the eruption have been selected to show a normal vertical structure of the perturbation. In these cases (green line in Figure 4b), the perturbation of atmospheric temperature is close to 0, indicating neutral conditions.

4. Summary and Discussion

We have described the results from the analysis of the microwave brightness temperatures from NOAA-20/SNPP ATMS and MetOp-B/MetOp-C AMSU-A and the MiRS retrieved atmospheric temperature a few hours after the initial volcanic eruption at Hunga Tonga-Hunga Ha'apai Tonga on 15 January 2022. The Hunga-Tonga outbreak created a valuable opportunity to study waves with very high phase speeds that otherwise have not been observed in the atmosphere yet. The present study is the first analysis of the vertical structure of these waves with satellite microwave measurements.

In this study, the atmospheric wave patterns generated by the Tonga volcanic eruption are clearly seen in the stratosphere for both the satellite microwave brightness temperatures and the MiRS retrieved atmospheric temperatures. While the perturbations are seen in all of the stratospheric sounding channels (i.e., channels 10–15 and 9–14 for ATMS and AMSU-A, respectively), the perturbation amplitude of the brightness temperature is the largest at channel 15 for ATMS and channel 14 for AMSU-A whose weighting function peaks have the highest altitude. As the channel weighting function peak altitude becomes lower, the amplitude of the atmospheric perturbation decreases. The microwave brightness temperature perturbation amplitude at ATMS channel 15 is about 1.7 K for the Lamb wave and about 1.9 K for the lead wave of the following gravity waves. Similar results were found for the MiRS retrieved atmospheric temperature. In other words, the amplitude of the perturbation

in the retrieved atmospheric temperature is larger in the upper stratosphere. The atmospheric wave pattern in the retrieved atmospheric temperatures can be observed down to approximately 50 hPa. The amplitude of the atmospheric wave in the retrieved atmospheric temperature at 2.5 hPa is about 2.0 K for the Lamb wave and about 2.3 K for the lead gravity wave that follows the Lamb wave. The vertical structure (i.e., magnitude and phase) of the perturbations seen for each of the waves analyzed are consistent with that predicted by theory (Bretherton, 1969; Fritts & Alexander, 2003; Swenson et al., 2000; Wright et al., 2022).

The high phase speed and in-phase vertical structure are revealed in the satellite microwave brightness temperatures and in the MiRS retrieved atmospheric temperatures for the Lamb wave. The lead gravity wave perturbation shows a similar behavior to the Lamb wave: the perturbation remains positive with decreasing amplitude in the stratosphere as the altitude decreases. Finally, for the trailing gravity waves located closer to the Tonga eruption location, the perturbation sign changes with altitude.

Data Availability Statement

NOAA-20/SNPP ATMS data are available from NOAA CLASS (https://www.avl.class.noaa.gov/saa/products/search?sub_id=0&datatype_family=ATMS_SDR&submit.x=32&submit.y=2 and https://www.avl.class.noaa.gov/saa/products/search?sub_id=0&datatype_family=ATMS_TDR&submit.x=30&submit.y=4), and MetOp-B/MetOp-C AMSU-A data are available from EUMETSAT (https://archive.eumetsat.int/usc/UserServicesClient.html). Users need to register through (https://eoportal.eumetsat.int/userMgmt/protected/welcome.faces) to access EUMETSAT. MiRS retrieval outputs (for all the satellites) are available from NOAA CLASS (https://www.avl.class.noaa.gov/saa/products/search?sub_id=0&datatype_family=JPSS_SND&submit.x=31&submit.y=5 and https://www.avl.class.noaa.gov/saa/products/search?sub_id=0&datatype_family=MIRS_MAP&submit.x=20&submit.y=4).

Acknowledgments
This work is supported by NOAA under Grant NA19NES4320002 to the Cooperative Institute for Satellite and Earth system Studies (CISESS) at the University of Maryland/Earth System Science Interdisciplinary Center (ESSIC). The manuscript contents are solely the opinions of the authors and do not constitute a statement of policy, decision, or position on behalf of NOAA or the U.S. government.

References

Alexander, M. J., & Barnet, C. (2007). Using satellite observations to constrain parameterizations of gravity wave effects for global models. *Journal of the Atmospheric Sciences*, *64*(5), 1654–1665. https://doi.org/10.1175/JAS3897.1

Boukabara, S.-A., Garrett, K., Chen, W., Iturbide-Sanchez, F., Grassotti, C., Kongoli, C., et al. (2011). MiRS: An all-weather 1DVAR satellilte data assimilation and retrieval system. *IEEE Transactions on Geoscience and Remote Sensing*, *49*(9), 3249–3272. https://doi.org/10.1109/TGRS.2011.2158438

Boukabara, S. A., Garrett, K., Grassotti, C., Iturbide-Sanchez, F., Chen, W., Jiang, Z., et al. (2013). A physical approach for a simultaneous retrieval of sounding, surface, hydrometeor, and cryospheric parameters from SNPP/ATMS. *Journal of Geophysical Research: Atmospheres*, *118*(22), 12600–12619. https://doi.org/10.1002/2013jd020448

Bretherton, F. P. (1969). Lamb waves in a nearly isothermal atmosphere. *Quarterly Journal of the Royal Meteorological Society*, *95*(406), 754–757. https://doi.org/10.1002/qj.49709540608

Carr, J. L., Horvath, A., Wu, D. L., & Friberg, M. D. (2022). Stereo plume height and motion retrievals for the record setting Hunga Tonga-Hunga Ha'apai eruption of 15 January 2022. *Geophysical Research Letters*, *49*(9), e2022GL098031. https://doi.org/10.1029/2022GL098131

Fritts, D. C., & Alexander, M. J. (2003). Gravity wave dynamics and effects in the middle atmosphere. *Reviews of Geophysics*, *41*(1), 1003. https://doi.org/10.1029/2001rg000106

Grassotti, C., Lee, Y.-K., Liu, S., & Liu, Q. (2019). Validated maturity science review for MiRS NOAA-20/ATMS algorithm. In *JPSS/SNPP Algorithm Maturity Matrix*. Retrieved from https://www.star.nesdis.noaa.gov/jpss/AlgorithmMaturity.php

Grassotti, C., Liu, Q., Lee, Y.-K., Liu, S., & Zhou, Y. (2023). Satellite microwave sounder product retrieval validation. *Field Measurements for Passive Environmental Remote Sensing*, *297*, 297–317. https://doi.org/10.1016/B978-0-12-823953-7.00018-6

Lee, Y.-K., Grassotti, C., Liu, Q., Liu, S., & Zhou, Y. (2022). In-Depth evaluation of MiRS total precipitable water from NOAA-20 ATMS using multiple reference data sets. *Earth and Space Science*, *9*(2), e2021EA002042. https://doi.org/10.1029/2021EA002042

Matoza, R. S., Fee, D., Assink, J. D., Iezzi, A. M., Green, D. N., Kim, K., et al. (2022). Atmospheric waves and global seismoacoustic observations of the January 2022 Hunga eruption, Tonga. *Science*, *377*(6601), 95–100. https://doi.org/10.1126/science.abo7063

Press, F., & Harkrider, D. (1966). Air-Sea waves from the explosion of Krakatoa. *Science*, *154*(3754), 1325–1327. https://doi.org/10.1126/science.154.3754.1325

Schoeberl, M. R., Wang, Y., Ueyama, R., Taha, G., Jensen, E., & Yu, W. (2022). Analysis and impact of the Hunga Tonga-Hunga Ha'apai stratospheric water vapor plume. *Geophysical Research Letters*, *49*(20), e2022GL100248. https://doi.org/10.1029/2022GL100248

Swenson, G. R., Alexander, M. J., & Haque, R. (2000). Dispersion imposed limits on atmospheric gravity waves in the mesosphere: Observation from OH airglow. *Geophysical Research Letters*, *27*(6), 875–878. https://doi.org/10.1029/1999gl010738

Wright, C. J., Hindley, N. P., Alexander, M. J., Barlow, M., Hoffmann, L., Mitchell, C. N., et al. (2022). Surface-to-space atmospheric waves from Hunga Tonga-Hunga Ha'apai eruption. *Nature*, *609*(7928), 741–746. https://doi.org/10.1038/s41586-022-05012-5

Wu, D. L. (2004). Mesoscale gravity wave variances from AMSU-A radiances. *Geophysical Research Letters*, *31*(12), L12114. https://doi.org/10.1029/2004GL019562

Zhang, K., Zhou, L., Goldberg, M., Liu, X., Wolf, W., Tan, C., & Liu, Q. (2017). A methodology to adjust ATMS observations for limb effect and its applications. *Journal of Geophysical Research: Atmospheres*, *122*(21), 11347–11356. https://doi.org/10.1002/2017JD026820

Zou, C.-Z., & Qian, H. (2016). Stratospheric temperature climate data record from merged SSU and AMSU-A observations. *Journal of Atmospheric and Oceanic Technology*, *33*(9), 1967–1984. https://doi.org/10.1175/JTECH-D-16-0018.1